Experimental and crystal plasticity study on deformation bands in single crystal and multi-crystal pure aluminium

Qinmeng Luan[a], Jun Jiang[a]*

a. Department of Mechanical Engineering, Imperial College London, London SW7 2AZ, UK

*Corresponding author. Email address: jun.jiang@imperial.ac.uk

Abstract

Deformation bands (DBs) formed in metals even in single crystals are known to give rise to the microstructural heterogeneities, thus contributing to some long-standing microstructure formation problems, such as the occurrence of recrystallization on the basis of deformed microstructure. Previous experimental transmission electron microscope (TEM) work has identified two types of DBs in the microscopic scale, i.e. kink bands and bands of secondary slips, showing the importance of understanding the slip activation for DBs. To extend the theory in mesoscale, single crystal and multi-crystal pure aluminium, as well as their corresponding crystal plasticity finite element (CPFE) models, are used in this paper to explore the effect of grain orientation, strain level and neighbouring grains on the formation of DBs. It is demonstrated that slip band intersection of primary and secondary slips is predicted to constrain the lattice sliding but facilitate the lattice rotation for the formation of DBs regarding the wall of DBs and its orientation. It is found that the impact of the above factors on the formation of DBs is caused by the slip field of primary slips. A sufficient amount of primary slips activated inside grains would be the key to the formation of distinct DBs with high area fraction and aspect ratio.

Keywords: deformation band, slip band intersection, crystal plasticity, pure aluminium

1 Introduction

The term deformation band (DB) defined by Barrett et al. [1] in 1939 describes a volume of approximately constant orientation that is significantly different from the orientation elsewhere in that grain. DBs are found in various alloys no matter in single crystal or polycrystalline structure, such as steel [2], zinc [3], aluminium [4], copper [5], nickel [6], magnesium [7], titanium [8] and etc. The formation of DBs is able to effectively accommodate the plastic strain and give rise to the heterogeneities in microstructure by forming noticeable orientation gradients and eventual fragmentation of grains [9]. Therefore, understanding the formation of DBs by examining its crystallographic features might be the key to understanding the grain nucleation in the recrystallization process regarding nucleation criteria and nucleated grain orientations on the basis of heterogeneous deformed microstructure.

The formation process of two kinds of DBs, i.e. kink bands and bands of secondary slip, was identified by etch pit tests and Laue back-reflection method with an X-ray beam in face centred cubic crystals (FCC) in tension in the 1990s by Higashida et al. [5]. These dislocation structures of two kinds of DBs observed by etch pit technique have an excellent agreement with the observations by transmission electron microscope (TEM) [10,11] and X-ray topography. The kink band is found to be a wall perpendicular to the primary slip direction and the band of secondary slips is a zone approximately parallel to the primary slip plane in which secondary slips are operating more actively than the primary slip [5]. Kink bands and bands of secondary slip are transmuted from the local bend-gliding regions and the coplanar slip zones of primary slips respectively. However, the orientations formed in DBs in mesoscale and factors affecting the shape and the amount of DBs are not clearly understood.

In some previous papers, the effect of grain orientation on the formation of DBs is studied for rolling as it is relevant to the generation of deformation textures [9,12]. For instance, the {110}<001> Goss orientation in FCC crystals is stable under rolling in single crystal and polycrystals with large grains, i.e. the Goss oriented grains can undergo extensive deformation without the development of large-scale heterogeneities [9]. By contrast, the Cube oriented FCC crystals are very heterogeneous under rolling for the formation of DBs [12]. The orientation in DBs is found by rotations about the transverse direction. However, the rotation direction and its reasons are not clearly addressed. Therefore, apart from the orientation formed in DBs, how the strain level and neighbouring grains affect the formation of DBs have not been systematically discussed. This long-standing problem retards the understanding of the subsequent microstructural evolution, such as recrystallization [13–15].

The development of recrystallized microstructure is affected by the formation and growth of nuclei in the deformed structure, while the grain nucleation is dominated by the rate of dislocation accumulation and heterogeneities of deformed structure [9,16]. In order to understand and predict the microstructural evolution during recrystallization and grain growth [17,18], it is essential to examine the development of the heterogeneities in the deformed state [9,13].

It is extremely important to thoroughly understand the formation of DBs for the study of recrystallization since it provides both the heterogeneous strain distribution and high orientation gradients regarding the crystallographic features. The amount of stored energy and orientation gradients after deformation would be important conditions for the formation of nucleation sites [21,22], affecting the recrystallization rate, recrystallized grain size and recrystallized orientation. For instance, single crystals that are deformed in single glide and recovered during annealing may not recrystallize. Because the dislocation structure which does

not contain the heterogeneities and orientation gradients cannot provide nucleation sites during annealing [9].

Furthermore, the formation of DBs is a crucial source of new orientations acquired for the deformed structure. In order to accurately predict the recrystallised texture [23] developed after grain nucleation and grain growth based on the deformed texture, understanding the deformed texture, *i.e.* orientation formed in DBs, could shed some lights on the orientations in the nucleus during recrystallization. For instance, in {100}<001> orientated silicon-iron single crystals, the recrystallized orientation kept the same with the orientation in the deformed structure which was {001}<210> [24].

In this paper, single crystals pure aluminium with four different orientations and multi-crystals with different grain morphology were compressed to 0.3 and 0.2 engineering strain. Crystal plasticity finite element (CPFE) models are developed to assess the experimental observations of DBs. Strain distributions were evaluated using the digital image correlation (DIC) technique [25–27] and applied to validate the CPFE model. Deformation activities were evaluated using optical microscopy and electron back-scattered diffraction (EBSD) for the slip lines and DBs, as well as the CPFE modelling for the effective plastic strain and primary slip field calculation. These results provide explanations for the observation in as a unified manner.

2 Experiment and CPFE model

2.1 Materials preparation

This work used two types of pure aluminium obtained by the Czochralski process [28] from Shanghai Jiaotong University (China) to study the formation of DBs: one is cubic single crystals with >99.999% purity (hereafter referred as 5N); the other one is cuboid columnar multi-crystals with >99.9% purity (hereafter referred as 3N). The chemical composition of 5N and 3N are listed in Table 1.

Table 1 Chemical composition of pure aluminium 5N and 3N used in this work

Sample (wt. %)	Al	Si	Ga	Zn	Fe	Cr	V	Mn	Zr
3N	99.9671	0.0048	0.0045	0.0045	0.0160	0.0009	0.0008	0.0007	0.0003
5N	99.9998	0.00009	0.00004	0.00001	0.00001	0.000004	0.00002	0.000003	0.00001

Face 1 and Face 2 of each sample for EBSD analysis were prepared metallographically with SiC papers (up to 1200 grit) and then polished with ~50 nm OP-S (Oxide Polishing Suspensions) diluted with H_2O by a ratio 1:5 of OP-S:H_2O. Each face was finally electropolished for 40s in a solution of 9.5 vol% perchloric acid in ethanol at room temperature and 20 V. The electropolished samples were immersed into 0.5 vol% hydrofluoric acid for 6 min to reveal its microstructure under an optical microscope.

2.2 Uniaxial compression tests and DIC

The uniaxial compression tests for 3N and 5N samples were carried by Instron mechanical testing frame to achieve up to 0.3 engineering strain at a 0.02 s^{-1} strain rate and room temperature. Sample geometries and stress-strain behaviours from experiments and CPFE modelling can be found in Figure 1. Samples were lubricated by the extremely stable lithium complex grease on both sides to reduce the friction during the compression.

Monochrome time-series 14 bit digital images were taken from the compressed front surface, by a Canon camera EOS 60D with the function of high-speed continuous shooting. The total number of pixels on the specimen is around 1.6×10^5. The correlation of time-series images for strain responses was performed using software GOM Correlate 2018[1] [29]. The facet size and point distance were set to be 19×19 pixels and 16 pixels with 15.6% overlapping, for the strain calculation. The facet matching was set against the first image with a single pass. The max. intersection deviation of 0.10 pixels and min. pattern quality of 1.10 were applied for this high accuracy mode. The interpolation method for subpixels was bicubic.

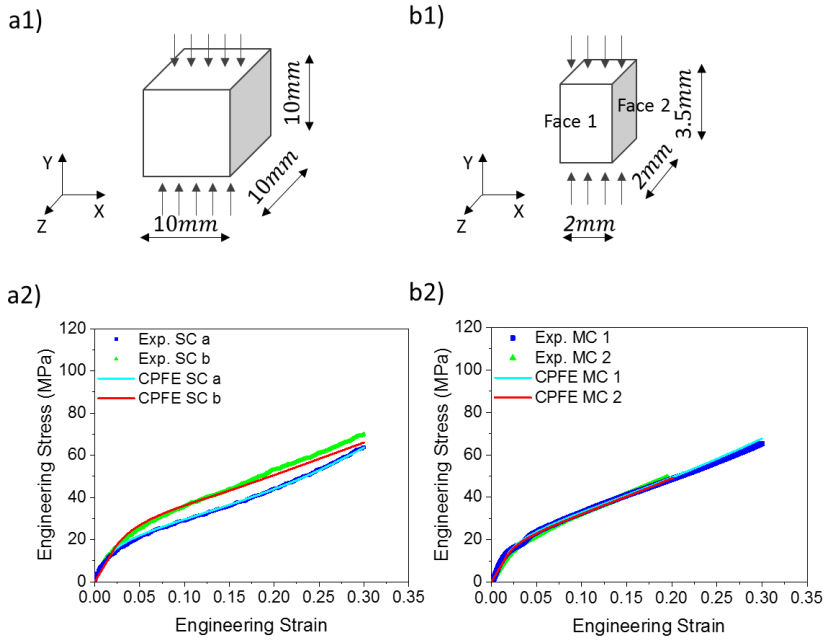

Figure 1 a1)-b1) show the sample geometry of single crystal (SC) and multi-crystal (MC) samples for testing. a2)-b2) shows the exp. and simulated engineering stress-strain curves of uniaxial deformed SC and MC.

2.3 Characterisation

Optical microscope and EBSD were applied for the microstructural characterisation. Images obtained under an optical microscope equipped with cross polarizers was interrogated using ImageJ software to clearly reveal the DBs. EBSD maps were captured on a Hitachi S3400N with Bruker eFlashHR EBSD system equipped with an eFlashHR camera and Esprit v2.1 software. An accelerating voltage of 20 kV and a step size of 3 µm were used for the EBSD mapping.

[1] https://www.gom-correlate.com/

2.4 CPFE model

The CPFE model [21,30] is able to capture the heterogeneities of stress and strain distribution, by taking into account of the elastic and plastic crystal anisotropy. The model used in this work is implemented in the UMAT subroutine of ABAQUS software using an explicit scheme.

The deformation gradient, **F**, is given by the sum of the elastic deformation gradient $\mathbf{F}^{\mathbf{e}}$ and plastic deformation gradient $\mathbf{F}^{\mathbf{p}}$. The rate of deformation, **D**, is given by the sum of elastic and plastic rates of deformation, $\mathbf{D}^{\mathbf{e}}$ and $\mathbf{D}^{\mathbf{p}}$. $\mathbf{D}^{\mathbf{e}}$ is determined by the anisotropic Hook's law and $\mathbf{D}^{\mathbf{p}}$ is determined from the symmetry component of plastic velocity gradient, $\mathbf{L}^{\mathbf{p}}$, as

$$\mathbf{D}^{\mathrm{p}} = \mathrm{sym}(\mathbf{L}^{\mathrm{p}}) \tag{1}$$

where $\mathbf{L}^{\mathbf{p}}$ is the sum of contribution to slips from the active slip systems expressed as

$$\mathbf{L}^{\mathrm{p}} = \sum_{\alpha=1}^{12} \dot{\gamma}^{\alpha} \mathbf{s}^{\alpha} \otimes \mathbf{n}^{\alpha} \tag{2}$$

where $\mathbf{s}^{\alpha}$ is the line vector along the slip direction and $\mathbf{n}^{\alpha}$ is its slip plane normal. The dislocation slip rate on the slip system α, $\dot{\gamma}^{\alpha}$, is given by

$$\dot{\gamma}^{\alpha} = \rho_{SSD}^{m} v b^2 \exp\left(-\frac{\Delta H}{kT}\right) \sinh\left(-\frac{\Delta V}{kT}\left|\tau^{\alpha} - \tau_c^{\alpha}\right|\right) \tag{3}$$

where ρ_{SSD}^{m} is the density of gliding statistically stored dislocations (SSD), v is the frequency to overcome obstacle barriers, b is the Burgers vector for FCC crystal, ΔH is the Helmholtz energy, k is the Boltzmann constant, T is the temperature in Kelvin, ΔV is the associated activation volume from literature, τ_c^{α} is the critical resolved shear stress for the slip system α. The accumulated slip after a certain period, $\gamma_{t+\Delta t}^{\alpha}$, is given by

$$\gamma_{t+\Delta t}^{\alpha} = \gamma_t^{\alpha} + \left|\dot{\gamma}_{t+\Delta t}^{\alpha}\right| \Delta t \tag{4}$$

A Taylor's dislocation hardening rule to describe the isotropic hardening during plastic deformation is expressed as

$$\tau_c^{\alpha} = \tau_{c0} + G_{12} \cdot b \cdot \sqrt{\rho_{SSD}^{s}} \tag{5}$$

where τ_{c0} is the initial critical resolved shear stress, G_{12} is the shear modulus, ρ_{SSD}^{S} is the density of sessile SSD determined by a phenomenological relation with effective plastic strain p as

$$\dot{\rho}_{SSD}^{\mathrm{s}} = \lambda \cdot \dot{p} \tag{6}$$

where λ is the work hardening coefficient and the effective plastic strain rate $\dot{p}$ is calculated from the plastic deformation rate tensor $\mathbf{D}^{\mathbf{p}}$ by

$$\dot{p} = \left(\frac{2}{3}\mathbf{D}^{\mathrm{p}} : \mathbf{D}^{\mathrm{p}}\right)^{1/2} \tag{7}$$

The physical properties used in this work for pure aluminium were obtained from the literature [30,31] and listed in Table 2. Note that the Helmholtz free energy ΔH used in this study did not consider the strain rate effect because the test is conducted at room temperature.

Table 2 Material properties of pure aluminium

Boltzmann constant (k)	1.38×10^{-23} JK^{-1}
Burgers vector magnitude (b)	2.86×10^{-4} µm
Temperature (T)	293 K
Young's modulus (E)	700 MPa
Initial slip stress (τ_c)	6 MPa
Mobile dislocation density (ρ_{SSD}^{m})	0.01 µm^{-2}
Jump frequency (v)	10^{11} s^{-1}
Helmholtz free energy (ΔH)	2.9×10^{-20} J
Activation volume (ΔV)	$6\times10^{-15}b^2$
Hardening coefficient (λ)	0.1 µm^{-2}
Strain rate ($\dot{\varepsilon}$)	2×10^{-3} s^{-1}
Possion's ratio (v_{12})	0.35

3D single crystal and multi-crystal CPFE models were constructed to study the deformation behaviour of pure aluminium. Finite elements with 20 nodes and reduced integration (C3D20R) were used. The orientation information in CPFE model was obtained directly from the corresponding EBSD maps. The bottom, left and back surfaces are fixed in the model to simulate the uniaxial compression to 0.2 and 0.3 engineering strain.

Commented [JJ1]: The boundary conditions are not clear here, could you clarify how you fixt the three planes

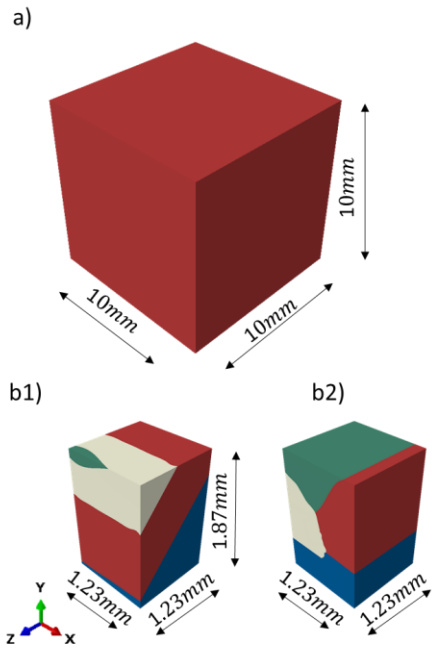

c)

Slip system	Slip plane	Slip direction
1	(111)	<1$\bar{1}$0>
2	(111)	<01$\bar{1}$>
3	(111)	<10$\bar{1}$>
4	($\bar{1}$11)	<011>
5	($\bar{1}$11)	<01$\bar{1}$>
6	($\bar{1}$11)	<101>
7	(1$\bar{1}$1)	<110>
8	(1$\bar{1}$1)	<011>
9	(1$\bar{1}$1)	<10$\bar{1}$>
10	(11$\bar{1}$)	<1$\bar{1}$0>
11	(11$\bar{1}$)	<011>
12	(11$\bar{1}$)	<101>

Figure 2 CPFE models for a) single crystals and b1)-b2) multi-crystals; c) shows the designations of 12 slip systems of aluminium FCC structure with respect to an orthogonal (x, y, z) reference system.

3 Experimental and modelling results

3.1 Validation of CPFE model

The simulated stress-strain curves shown in Figure 1 gives reasonably good agreement with experimental data for both single crystals and multi-crystals. Note that there is a very slight stress drop in the stress-strain curve for MC 1 at ~0.06 strain. By checking the deformed shape of MC 1, the slight shift of stress could be attributed to the generation of obvious slip lines (i.e. shifts of lattice structure to sample surface).

In addition, the DIC experimental and CPFE numerical strain yy maps, for deformed single crystal and columnar multi-crystal samples, show a good match, when the total engineering strain is 0.15 and 0.3. The distribution of strain yy on the midline of deformed single crystals and multicrystal is shown in Figure 3a). The spread of strains along the midline is shown by their standard deviation as error bars in Figure 3 a). The shape of deformed single crystals are also compared with the deformed CPFE models in Figure 3 b) and c). The above comparisons made between experimental results and CPFE simulated results demonstrate that our CPFE model is able to simulate the deformation behaviour of single, multi-crystal pure aluminium alloys with reasonable accuracy.

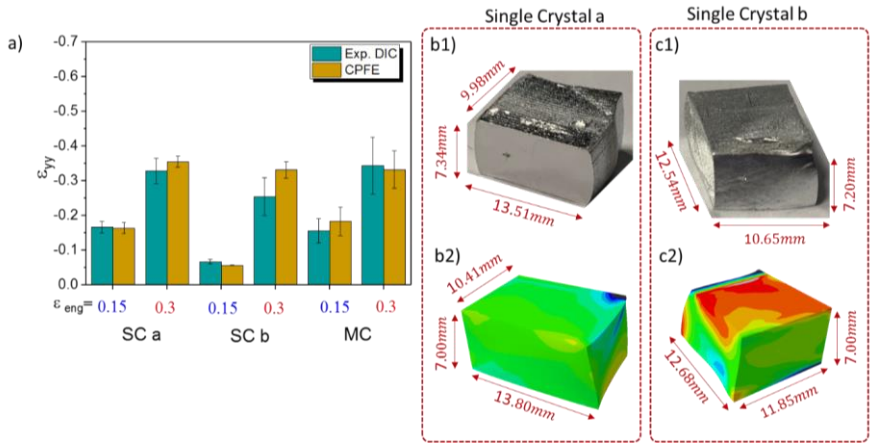

Figure 3 a) Comparison of average ε_{yy} on the midline of the specimen between DIC calculated and CPFE simulated results when the overall engineering strain is 0.15 and 0.3. b1)-b2) and c1)-c2) compare the geometry of deformed samples from experiments and CPFE simulations.

3.2 Single crystal analysis

3.2.1 Slip trace analysis

The slip field of the activated slip systems and their slip traces left on the XY face were calculated by CPFE modelling for the single crystal a, b, c and d (see Figure 2). Two types of slip lines with different tilting angles were plotted superimposed with the traces of four slip planes. OM results also show that slip line 1 and 2 are more closely aligned with the traces of slip systems with the highest and second-highest value of slip field (i.e. primary and secondary slip system) in all deformed single crystals. It is rational that some slip lines are not perfectly aligned with their corresponding {111} slip plane traces, as the slip trace analysis is based on

the initial undeformed crystal orientation while the observed slip lines are formed and rotated during the plastic deformation as the discussion in [32].

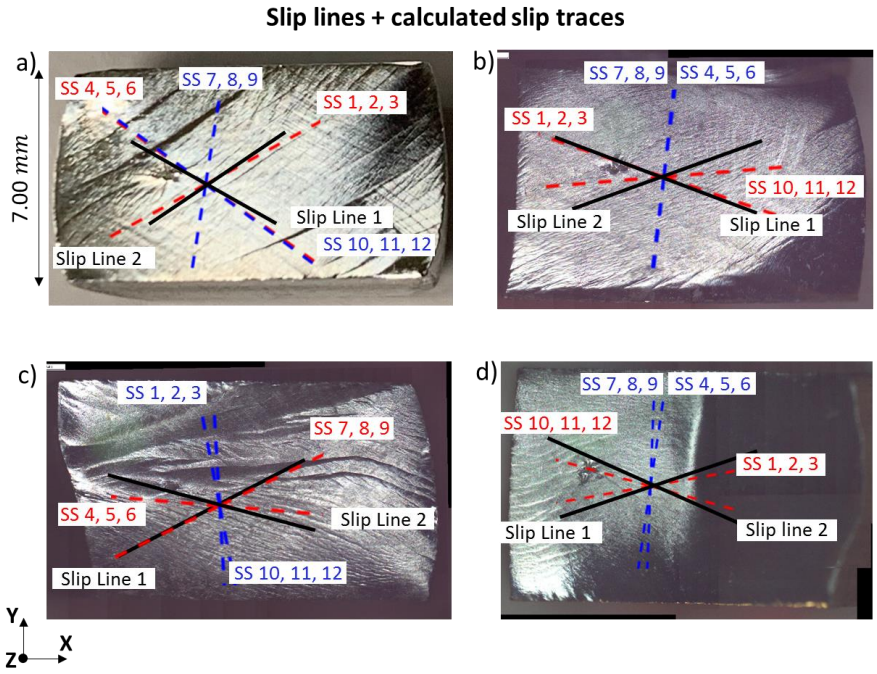

Figure 4 a)-d) are the optical microscope images of 30% uniaxial deformed single crystal a-d. Slip lines left on the sample surface and the calculated traces of 12 {111}<110> slip systems (SS) are superimposed. Traces of primary and secondary slips are highlighted in red and the other {111} traces are marked with blue dashed lines.

Commented [JJ2]: chanage the font of your caption to differ from the text

Commented [LQ3R2]: Changed. What about now?

3.2.2 Deformation band formation

The EBSD IPF maps according to the deformation axis (i.e. Y-axis) before and after deformation are plotted superimposed with their orientated crystals in Figure 5 a1)-d1). It can be seen that the DBs are formed in these crystals to accommodate the imposed plastic deformation. Unlike the uniaxial tension tests, the top and bottom surfaces of the compressed specimens are free to move horizontally as shown in [7]. The orientation of the matrix nearly remains the same before and after compression. The slight rotation of crystal orientation in the deformed matrix observed in Figure 5 could be attributed to the errors from sample preparation and imaging alignment.

DBs with similar tilting angles are found in deformed microstructure for each grain orientation (see Figure 5 a2)-d2)). Those bands are more likely located parallel to the slip line 2, such as single crystal a, b and c. The secondary slip system for every single crystal and its corresponding slip lines are determined and shown in Figure 5 a1)-d1).

After measuring the misorientation angle across the bands in Figure 5 a3)-d3), a sharp orientation change was observed at each edge of bands (i.e. deformation-induced grain boundary, see Figure 5 a4)-d4)). The misorientation >15˚ (i.e. HAGB) is developed during deformation for the deformation-induced grain boundary. This means the orientation inside the band has an approximately constant orientation that is significantly different from the orientation in the matrix. These observations agree with the definition of DBs by Barrett et al. [1] in 1939.

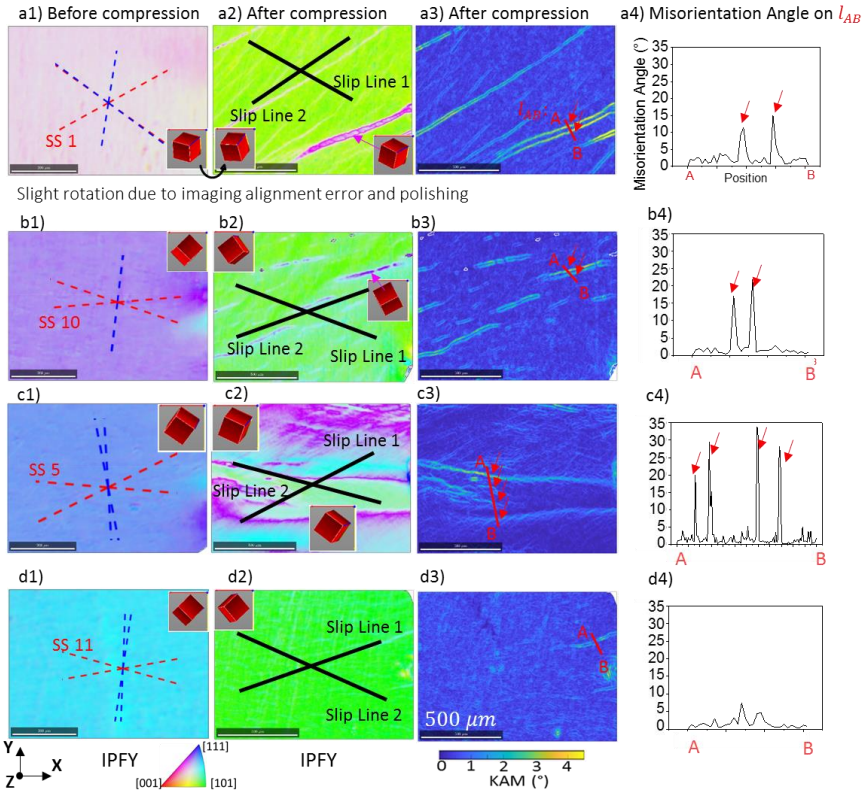

Figure 5 a1)-d1) and a2)-d2) are the EBSD IPF maps in the Y-axis (i.e. the loading direction) for the single crystal a-d before and after uniaxial compression. The secondary slip system (SS) and its trace are marked out as a comparison of slip line 2. a3)-d3) are the kernel average misorientation (KAM) maps of deformed single crystal a-d respectively. The misorientation distribution on Line AB is plotted in a4)-d4).

3.2.3 Single crystal modelling

CPFE predicted effective plastic strain and slip fields for the primary and secondary slip system are plotted for the front (i.e. XY) faces of deformed SC a, b, c and d in Figure 6. The existence of slip fields demonstrates that slip systems >1 are activated in deformed single crystals. The ellipsoidal DB is characterised by its aspect ratio a/2c, where a and c are the longer and shorter

length of semi-axes on the DB as shown in Figure 10 f). By comparing the slip fields in deformed SC a, b, c and d, it has been found that the primary slip exceptionally dominates in SC a, while it has the highest a/2c ratios of DBs (see Figure 10 e). Also, the primary slip is much less dominated in SC d while it has the fewest DBs (see Figure 5 and Figure 6 d).

Commented [JJ4]: define this new term

Commented [LQ5R4]: Defined as above

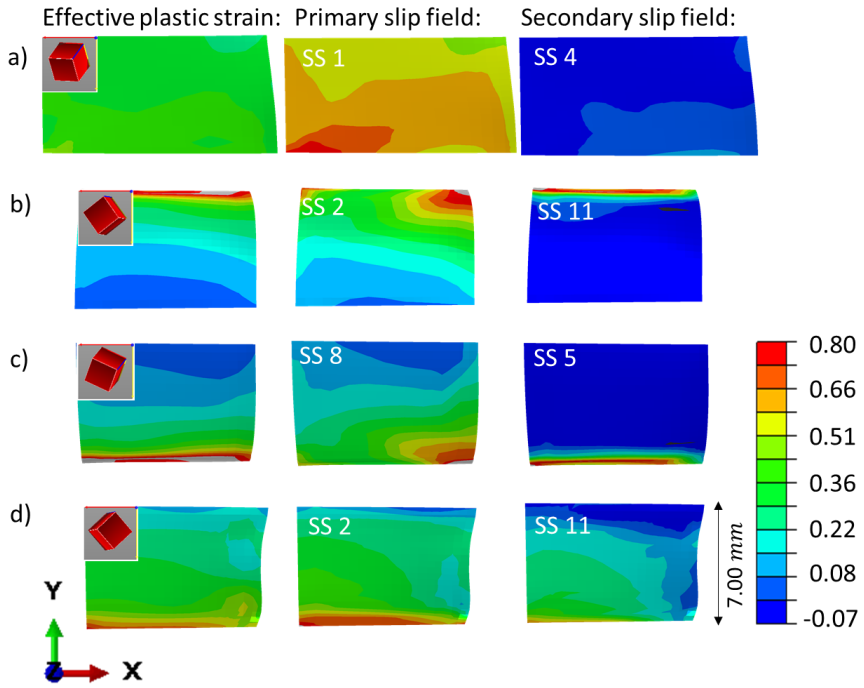

Figure 6 a)-d) are crystal plasticity predicted effective plastic strain distribution and slip fields for the primary and secondary slip system in single-crystal a, b, c and d.

In Figure 7, DBs left on the front (i.e. XY) face and b1) side (i.e. YZ) face of SC b and its CPFE results are compared. It has been shown from Figure 7 a) that the effective plastic strain distribution, primary and secondary slip fields vary for different faces of the same crystal. Figure 7 b1-2) and c1-2) are the OM images to show slip lines and etched DBs for the front (i.e. ZY) face and the side (i.e. XY) face respectively. It has been found that DBs are aligned nearly parallel to the secondary slip lines. It is very interesting to see the fraction of DBs and spacing between DBs are strongly correlated with the intensity of the primary slip field (see Figure 7 d1)-d2)). The higher the intensity of the primary slip field is, the higher the DBs fraction and the denser the DBs would be formed.

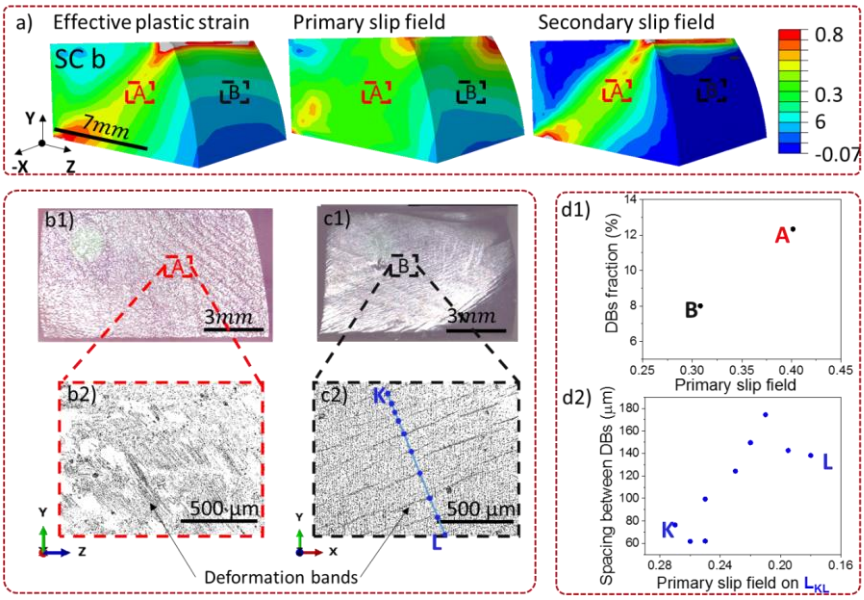

Figure 7 a) shows the CPFE calculated effective plastic strain distribution, primary slip field and secondary slip field for SC b. b1-2) and c1-2) are the OM images on side (i.e. ZY) face and front (i.e. XY) face respectively to show slip lines and etched microstructure. d1) compares the DBs fraction against its primary slip field. KL is a line vertical to the alignment of DBs with blue dots showing the nonuniform distributed DBs on Line KL. d2) quantitatively compares the spacing between adjacent DBs on Line KL against the CPFE simulated primary slip field at the corresponding position.

3.2.4 Orientation formation

Pole figures (PF) of {111} planes in deformed single crystals are plotted together with the PF before deformation in Figure 8 a1)-d1). Pole figures of {100} and {110} planes are shown in Appendix Figure B. It is clearly seen that the newly formed orientation is originated due to the rotation of matrix around Z-axis during deformation in Figure 8 a1)-d1). This indicates that the crystal slip planes are rotating around the loading axis. In Figure 8 a2)-d2), obvious orientation shifts (i.e. misorientation angle > 10˚) are also found in the deformation state resulting in the increase of misorientation angle distribution, especially for the crystals with distinct DBs, i.e. single crystal a, b and c. The increase of misorientation angle demonstrates that lattice sliding was not uniform even in this single crystal uniaxial compression due to the interaction of multiple slip systems, giving rise to the storage of dislocations in the deformed structure.

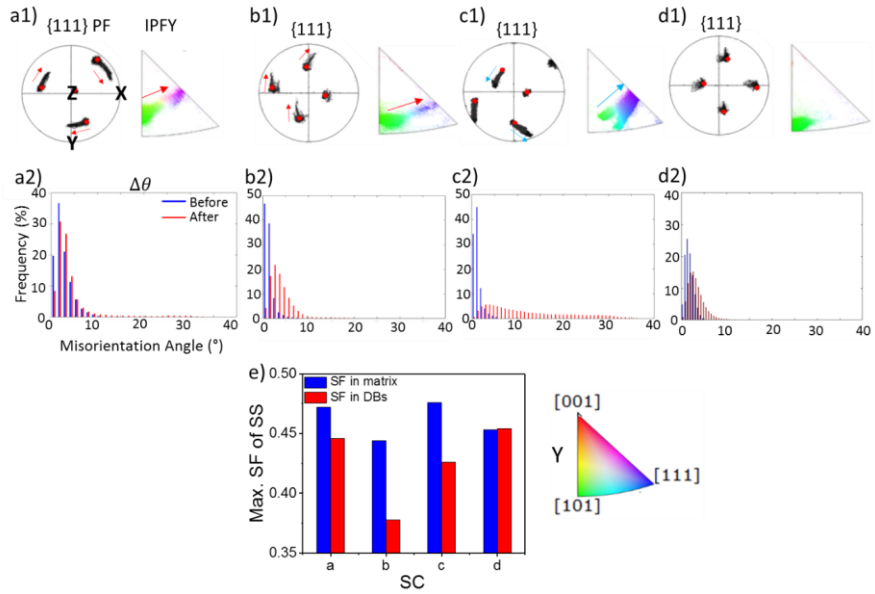

Figure 8 a1)-d1) are the pole figure (PF) and inverse pole figures (IPF) of deformed single crystal a-d. Red dots show the orientation before compression. Red arrows represent the clockwise rotation and blue arrows represent anti-clockwise rotation around Z-axis. The colour in IPF is consistent with IPF colour key regarding the compression direction (i.e. Y-axis). a2)-d2) show misorientation angle distribution before and after compression for single crystal a-d).

Through checking the corresponding inverse pole figures (IPF) in Figure 8 a2)-d2), it has been found that the {111} slip planes tend to orientate perpendicular to the loading direction (i.e. Y-axis) in the newly formed DB, which means slips become harder to be activated in DB (see Figure 8 a1)-d1)). This is confirmed by the drop in the highest Schmid factors (SF) in Figure 8 e) that the orientation in DBs is rotated to a 'harder' orientation. The Schmid factors of 12 slip systems in the deformed matrix and DBs are shown in Appendix Figure A.

3.3 Columnar multi-crystal

3.3.1 Slip trace and deformation band

The slip traces of 12 {111} <110> slip systems in each grain were calculated and plotted superimposed with the inverse pole figure (IPF) maps regarding the Y-axis (i.e. the loading direction) in Figure 9. The traces of two slip planes with the primary and secondary slip system calculated based on the CPFE are highlighted in red, and the other two {111} traces are highlighted with blue dashed lines. The most easily activated slip plane is labelled out by red, and the second easily activated slip plane is labelled out by black in Figure 9.

It can be seen in the EBSD estimated KAM maps that DBs with high misorientation angle on its transition bands were formed in some grains. By comparing the side (i.e. YZ) faces of MC 1 and 2 in Figure 9 a2)-b2), it can be concluded that the total imposed strain level does have a strong effect on the formation of DBs. The side faces of MC 1 and 2 have the same grain

orientations and tilting angle of GBs but different engineering strain levels, i.e. 0.3 for MC 1 and 0.2 for MC 2. The side face of MC 1 with the higher imposed strain has more distinct DBs, while no obvious DB is found in the side face of MC 2. The same with the study on single crystals, the specific factors causing the formation of DBs in multi-crystals are discussed by CPFE modelling in the next section.

Also, in these two MC samples that DBs are located in parallel to the secondary slip plane, especially on the front face of MC 1 and 2 (see Figure 9 a1)-b1)). However, DBs on side face are not perfectly aligned along the secondary slip plane. This might be due to the local stress field generated due to the presence of their neighbouring grains (see Figure 9 a2)-b2)).

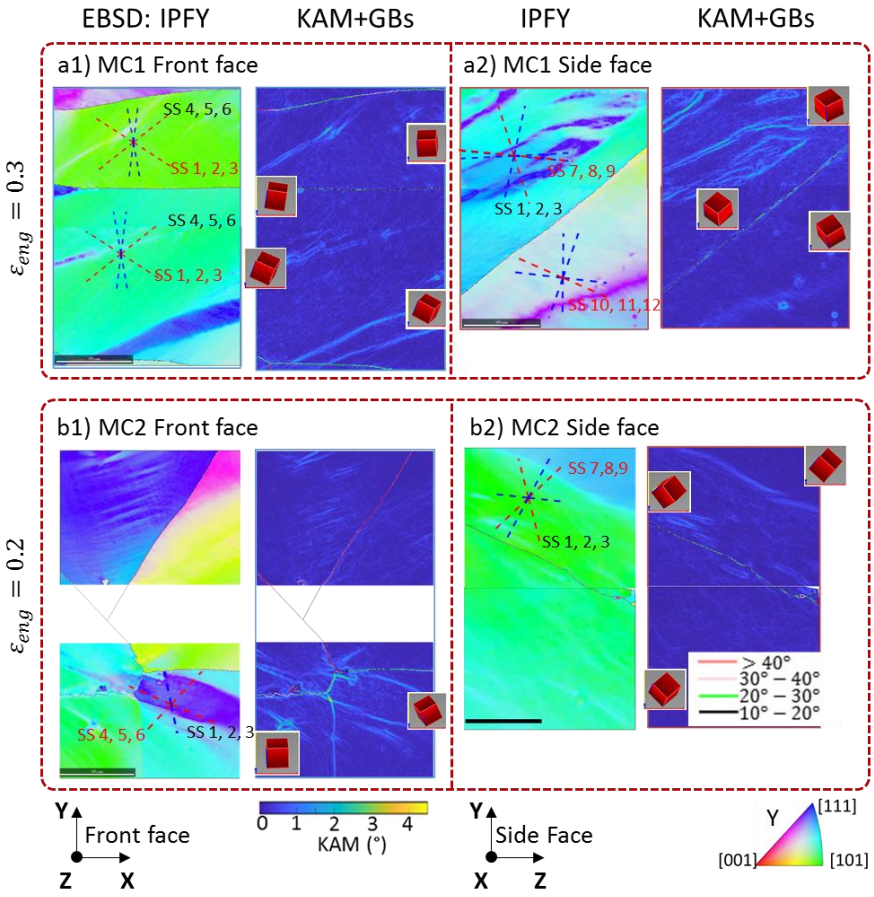

Figure 9 a1)-a2) and b1)-b2) show the EBSD IPF-Y map and its KAM map for front and side face on MC 1 and 2 respectively. The trace of primary and secondary slip plane are marked out as red dashed line together with the red and black label respectively in IPFY maps. The colour on grain boundaries

(GBs) in KAM maps indicates the value of misorientation on GBs. The crystal orientation information at each position is superimposed in the KAM maps.

3.3.2 Multi-crystal modelling

The effective plastic strain and slip field of primary slip on the front and side face is plotted in Figure 10 for CPFE multi-crystal (MC) 1 and 2 which were deformed to 0.3 and 0.2 engineering strain respectively. It is clear that the distribution of the effective (the sum of) plastic strain field is very different from the primary or secondary slip field.

By comparing the simulated results of the two set of microstructure in Figure 9, it is convincing that, instead of the effective plastic strain field, it is the primary slip field which is more correlative with the formation of DBs. For instance, the effective plastic strain distribution is quite homogeneous in the side face of MC 1. However, DBs shown in deformed EBSD maps were only formed in the above grain (i.e. grain ②). Also, the effective plastic distribution in the grain ④ on the front face of deformed MC 2 (see Figure 10 a2)) is low. However, a distinct DB is found in this area. By contrast, the primary slip field explains well for the formation of DBs, i.e. the higher the primary slip field, the more possible the DBs could be formed in this area.

Based on the work of Brown et at. [33], the DBs resulting from plastic strain would be ellipsoidal to balance the applied stress. The stress in the neighbourhood of the tip due to the dislocation pile-up would be proportional to the aspect ratio a/2c of the DBs (see the sketch in Figure 10 f). The relationship between the a/2c ratio of DBs and primary slip field, as well as effective plastic strain, are compared for deformed single crystals and multi-crystals in Figure 10 e) and f). The primary slip field demonstrates a strong correlation with the a/2c ratio of DBs, while no obvious relation is found between the effective plastic strain and a/2c ratio.

The DBs fractions on each face of MC 1 and 2 versus values of the effective plastic strain and primary slip field at the corresponding positions of DBs are plotted in Figure 10 g). It has been found that high DBs fraction is related to high values of the primary slip field, instead of the field of effective plastic strain.

Commented [JJ6]: Add him as the suggested reviewer

Commented [LQ7R6]: Okay

Commented [JJ8]: Good!

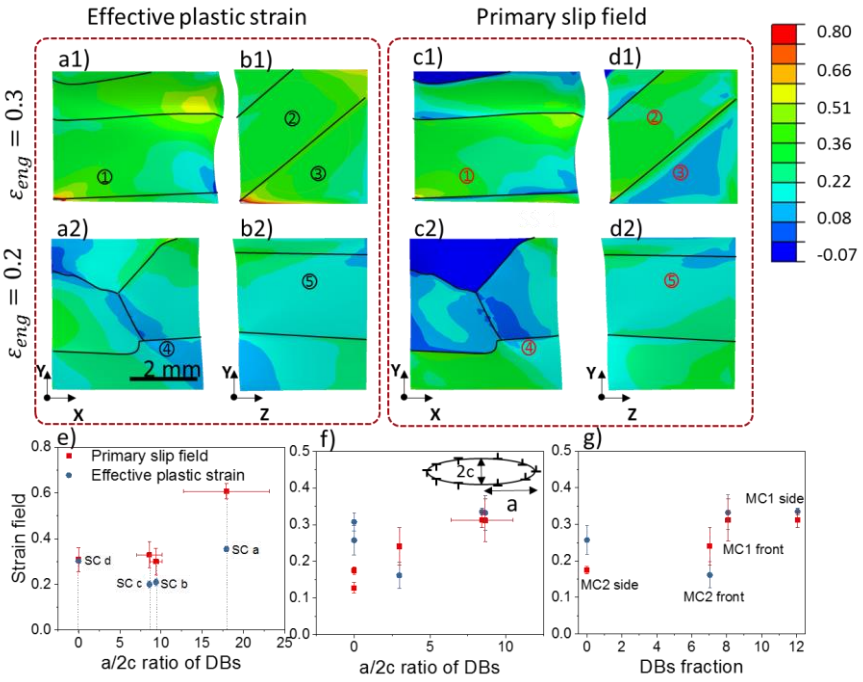

Figure 10 Crystal plasticity predicted effective plastic strain and primary slip fields for multi-crystals: a1)-b1), c1)-d1) are the front face and the side face of MC 1 which was deformed to 0.3 engineering strain; a2)-b2), c2)-d2) are front face and the side face of MC 2 which was deformed to 0.2 engineering strain. An ellipsoidal DB with semi-axes a and c is drawn after Brown et al. [33]. *e) and f) show a/2c ratios of DBs against primary slip field and effective plastic strain value in SC a-d and MC 1-2. g) shows DBs fractions against primary slip field and primary slip field for each face of multi-crystals. a/2c ratios and DBs fractions of the whole map are measured from EBSD maps while the primary slip field and effective plastic strain are obtained from CPFE modelling at the corresponding position.*

3.3.3 Orientation formation

Pole figures (PF) of each grain in deformed samples are plotted together with the PF of undeformed crystal in Appendix Figure C. Same with the DBs in deformed single crystals, obvious orientation rotations around Z-axis are found in the distinct DBs in deformed multi-crystals.

The corresponding inverse pole figures (IPF) regarding Y-axis for front and side face are plotted in Appendix Figure D for deformed MC 1 and 2. Keeping the same with the DBs in single crystals, the {111} slip planes in DBs are found to preferentially orientate perpendicular to the loading direction during compression, which means their slips are harder to be activated.

4 Discussions

In 1979, the homogeneous distribution of primary and secondary slip lines all over the sample area was already observed by Franciosi et. al. [34] in copper and aluminium single crystals under optical microscopes. These crystallographic slip lines were also found by Asaro [20] in 1983 in polycrystalline alloys. Gioacchino and Fonseca [32] in 2012 firstly related the local strain saturation with slip bands (i.e. with respect to slip lines) by using the digital image correlation technique. However, the mechanism of DBs formations has not been clearly understood by relating the slip system activation with the strain localisation. This work has systematically analysed the formation of DBs and its characteristics in single crystal and multi-crystal pure aluminium according to the slip trace analysis, EBSD mapping and crystal plasticity simulation.

4.1 Mechanism of deformation band formation

In this study, the tabular strain localisation structures defined as DBs are found in uniaxial compressed single crystal and multi-crystal pure aluminium alloys. Through comparing the optical microscope and EBSD maps of all samples at the same area before and after compression (see Figure 5), grain sliding and lattice rotation >15˚ are observed for the deformed sample matrix and DBs respectively.

According to the slip trace analysis shown in Figure 4, two types of slip lines are proven to be created by the primary and secondary slip system. The EBSD maps show that the DBs tend to align parallel to the trace left by the secondary slip system. (see Figure 5 for single crystals and Figure 9 for multi-crystals).

Therefore, it can be concluded that the slip band intersection of the the primary and secondary slip system could be the cause for the DB formation since the lattice sliding would be constrained at the slip band intersection area. Meanwhile, similarly with the Eshelby's model for the slip band and grain boundary intersections [35], the dislocations would pile up at the slip band intersection area giving rise to the high stress ahead of the blocked slip band. This local constraint prohibits the lattice sliding but would trigger lattice orientation rotation to form DBs. These observed DBs in mesoscale can be referred to kink bands rather than the bands of secondary slip since the wall of bands is perpendicular to the primary main slip direction as discussed in [5,7].

The mechanism of DB formation is summarised in Figure 11. Three different types of deformation in single crystal are shown in Figure 11 b): i) describes the lattice sliding (i.e. no orientation change) when only one slip system is activated; ii) describes the single slip system activation and lattice rotation (i.e. tilting) due to constraints; iii) describes the DBs formation due to slip band intersection. In Figure 11 c), a detailed sketch shows the intersection of two types of activated slip systems (i.e. *red* and *black* symbol), as well as the dislocation pile-up at the intersection point along with the secondary slip system. It also explains the strain localisation at the boundary of DBs due to the effective barriers to the dislocation motion, which is similar to the effect of grain boundaries [35].

Commented [JJ9]: The reference free style does not go well in the discussion section. It is meant to explain your results and discuss with previous research

Commented [LQ10R9]: Added the above paragraph for the comparison with the literature.

Commented [JJ11]: Remove or change as this should not be the fundamental reseason

Commented [LQ12R11]: Changed the GB effect to orientation change effect

Commented [LQ13]: Link to the literature

Commented [LQ14]: Newly added

Commented [LQ15]: Newly added

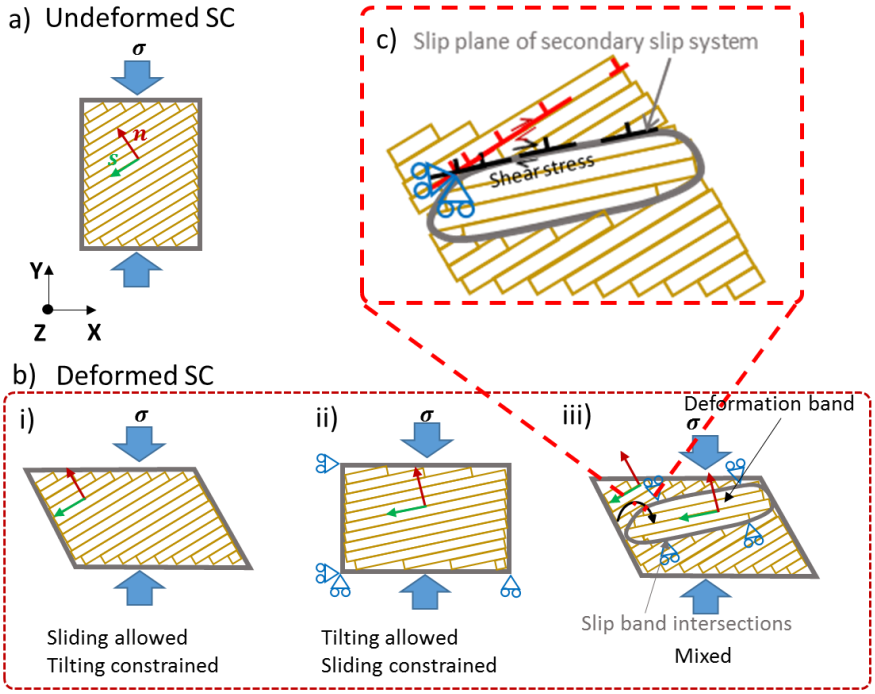

*Figure 11 A sketch to show the mechanism of DB formation. a) Slip direction **s** and slip normal **n** in a single crystal (SC) before deformation. b) Three types of deformation in deformed single crystal: i) lattice sliding only; ii) lattice rotation (i.e. tilting) with constraints; iii) a combination of lattice sliding and rotation due to local constraints causing the formation of DB. c) A detailed sketch shows the local constraint due to slip band intersection and dislocation pile up at an intersection point.*

4.2 Factors affecting deformation band formation

4.2.1 Crystal orientation

The deformed microstructures of four single crystals with different orientations are compared to study the effect of orientation on DB formation (see Figure 5). No distinct DBs are found in deformed single crystal (SC) d. By comparing the predicted effective plastic strain and slip field of single crystals in Figure 6, it can be seen that the SC a, b, c, d have similar values of effective plastic strain near DBs. Meanwhile, SC d has the most homogeneous slip field distribution for the primary and secondary slip systems (i.e. no dominating slip system) in comparison with the other single crystals. Therefore, when the total strain is the same, the crystal orientation would affect the formation of DBs by having a different level of primary slip fields. If one slip system is dominated during deformation, the peak value of its slip field, i.e. the value of primary slip field, could be high enough to facilitate the formation of distinct DBs with high misorientation on its boundaries (see SC a and b in Figure 5).

Furthermore, the crystal orientation also affects the aspect ratio, i.e. a/2c value, of formed DBs by having different levels of the primary slip field (shown in Figure 10 e). The primary slip

field could be directly related to the stress level formed at the tip of DBs while the stress is proportional to the aspect ratio a/2c of the DBs as discussed by Brown [33]. Therefore, the primary slip field has a strong correlation with the aspect ratio of DBs.

4.2.2 Strain level

The multi-crystals MC 1 and MC 2 which has nearly the same orientations were compressed to different strain levels, i.e. 0.3 engineering strain for MC 1 and 0.2 for MC 2, to compare the strain effect on DBs formation. Regarding the side faces of MC 1 and 2 whose grain orientation and grain structure are same, much fewer DBs and minor crystal rotation were found in MC 2 as seen in Figure 9 b1)-b2). Therefore, the induced strain level could also be the key factor in the formation of DBs. As shown by the CPFE results for side faces of MC 1 and MC 2 in Figure 10, the side face of MC 2 with no DBs have a lower value of the primary slip field while no obvious difference is found for the effective plastic strain level, especially in grain ②. Hence. the more primary slips would lead to more slip band intersection and the crystal rotation in DBs.

By comparing the aspect ratio a/2c of DBs in deformed MC 1 and MC 2, it has been found in Figure 10 f) that the high value of the primary slip field would prompt the occurrence of DBs with the high a/2c ratio. It may imply that highly concentrated stress could be formed at the tip of DBs due to the dislocation pile-up of primary slips.

4.2.3 Neighbouring grain

The grain structure could affect DBs formation due to the constraints imposed by the sharp sloped orientation change from neighbouring grains [32,36]. As discussed before, DBs formed in single crystals and multi-crystals are found to preferentially locate parallel to the slip trace of secondary slip system. However, for the side face of multi-crystals which have highly sloped orientation change, DBs are found to be parallel to the grain boundary instead of the secondary slip system (see Figure 9 a2)-b2)). Hence, the constraint imposed by the orientation change would affect the local stress-strain state in grains and lead to crystal rotation. The stress concentration at grain boundaries caused by slip band-grain boundary intersections has already been demonstrated by Guo et. al. [35] by using cross-correlation-based electron backscatter diffraction. The effect of neighbouring grains explains why DBs near the highly sloped grain boundary do not always in parallel to the secondary slip system.

However, it has been found that neighbouring grains would not affect the new orientation formed in DBs. The orientation in DBs near highly sloped grain boundary still tends to rotate around Z-axis and become ‘harder’ (see Figure D in Appendix).

4.2.4 Slip direction

The activated slip direction is also found to affect the formation of DBs, as the area fraction of DBs varies for the font face and side face of the same single crystal (see Figure 7 b)-d)). The grain orientation and total strain level are the same in this case. Therefore, the accumulation of slips on different faces would be different due to the activated slip direction, resulting in the different distribution of the primary slip field as shown in Figure 7 a). According to the quantitative analysis in Figure 7 d1)-d2), the higher the primary slip field is, the higher the area fraction of DBs and the higher density of DBs would be formed.

4.3 Orientation in deformation band

The orientation formed in DBs is analysed by comparing the pole figures and inverse pole figures of single crystals and multi-crystals before and after compression. According to the

Commented [JJ16]: Logic is not clear in this section, revise

Commented [LQ17R16]: Revised the whole section

Commented [LQ18]: Revised

Commented [LQ19]: Newly added

Commented [JJ20]: This part is not clear to me. Do you need this part~?

Commented [LQ21R20]: I moved this part as the last factor. I feel the conclusion from this part is a bit repeatable, but the factor: slip direction cannot be ignored. How do you think?

pole figures shown in Figure 8 and Figure D in the Appendix, it has been found that the orientation in DBs is formed due to the lattice rotation around Z-axis following clockwise or anti-clockwise direction. The more distinct DBs are formed, the higher the misorientation angle is found between the deformed matrix and DBs (see Figure 5 a4)-d4)).

According to the inverse pole figures (see Figure 8 a1)-d1) and Figure D in Appendix), it has been found that {111} slip planes in DBs tend to rotate perpendicular to the loading direction, i.e. Y-axis. This means that slips become harder to be activated in all DBs compared with the deformed matrix when the loading direction is still Y-axis. This has been demonstrated by the drop in the highest Schmid factors (SF) in DBs (see Figure 8 e)). Therefore, it is rational to conclude that the direction of crystal rotation in DBs, i.e. either clockwise or anti-clockwise, depends on which way could reduce its Schmid factor values. Furthermore, the higher the primary slip field is, the higher the rotation angle is found for the slip planes in DBs (i.e. the slips become 'harder' to be activated).

Commented [JJ22]: The DB slip planes may not rotate. They just formed in this manner

Commented [LQ23R22]: I think the slip planes are rotating during deformation. Because the roatation angle is increasing if we increase the strain level (i.e. primary slip field).

Commented [LQ24]: Added

4.4 Prediction on DBs

To perdicit the DBs formation, the CPFE modelling is a very effective technique, as the slip field of each slip system in single crystal, multi-crystals and polycrsytals can be checked. The primary slip field rather than the effective strain field can be used to determine whether distinct DBs would be formed in grains. As the DBs tend to occur at the high slip field regions, the primary slip field calculated based on crystal plasticity theory is helpful for the prediction on the area fraction, density and aspect a/2c ratio of activated DBs. As the CPFE modelling for the prediction of strain fields has been validated to a large extence by Dunne et. al. [30,31,37,38], the effect of neighbouring grains, complex strain path and strain levels can be simulated in mesoscale, to obtain the eventuated plastic strain distribution and the peak value of slip field.

5 Conclusions

In this work, integrated experimental study and CPFE modelling in mesoscale are utilized to provide new insights in understanding the mechanism of DBs formation in pure aluminium and its affecting factors. It has been shown that:

1. The DBs are produced aligning parallel to the secondary slip system due to the constraints from the slip band intersection of primary and secondary slips. It is rational to speculate that the lattice sliding is prohibited at the intersection area while the lattice rotation is triggered to form high angle grain boundaries (i.e. HAGBs) for DBs.
2. The orientation formed in the DBs is found to become harder since {111} slip planes in the DBs are much more likely to become perpendicular to the loading direction. Hence, the orientation formed in DBs can be estimated according to the initial grain orientation and primary slip field calculated from the CPFE modelling.
3. Various factors, including crystal orientation, strain level, neighbouring grains and slip direction, have an impact on the formation of DBs by affecting the primary slip field. DBs are formed preferentially in grains whose primary slip field rather than effective strain field reaches to criteria.
4. The value of the primary slip field has a strong correlation with the area fraction, aspect ratio (i.e. a/2c) and the density of formed DBs in deformed single crystal and multi-crystal pure aluminium alloys.

Author Contributions

QL devised this work and conducted mechanical testing, microstructure characterisation, CPFE modelling and data analysis. JJ supervised the work. QL and JJ contributed to drafting the final manuscript.

Acknowledgements

The strong support from the Aviation Industry Corporation of China (AVIC), the First Aircraft Institute (FAI), China Scholarship Council (CSC), the Henry Lester Trust and the Great Britain-China Educational Trust for this funded research is much appreciated. The research was performed at the AVIC Centre for Structural Design and Manufacture at Imperial College London. QL would also like to thank Dr Ruth Brooker for training and support of instrument usage, gratefully thank Dr Zebang Zheng, Dr Junyi Lee, Dr Bo Chen for their assistance on CPFE modelling and Ruiqiang Zhang for the assistance on DIC. Dr. Jun Jiang thank EPSRC for the funding the LightForm program: EP/R001715/1

Appendix

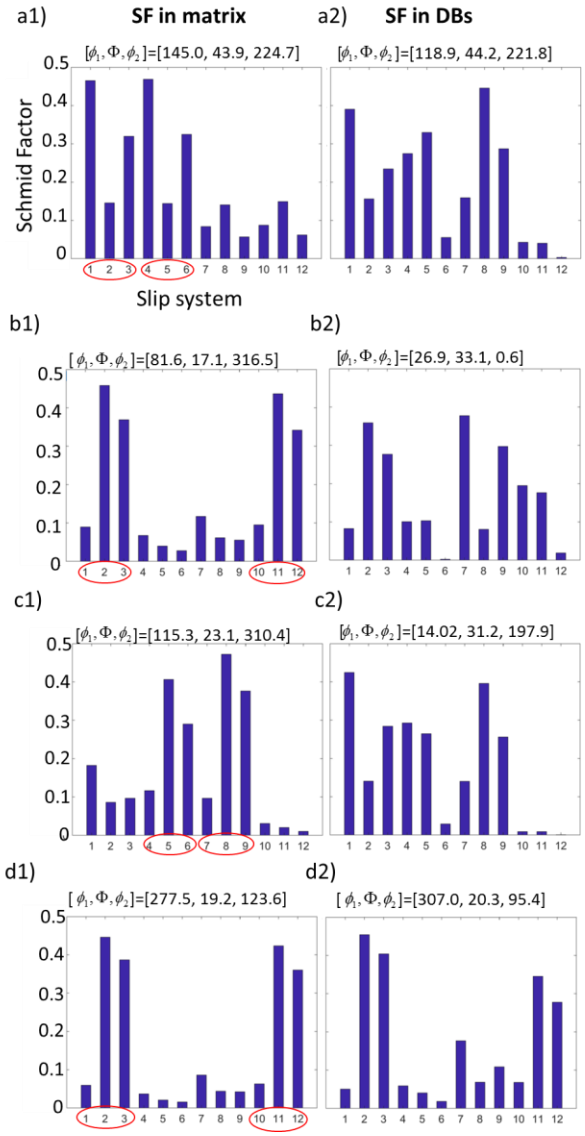

Figure A a1)-d1) are the calculation of Schmid factors for grain orientations of SC a, b c and d in the matrix. The most easily activated two slip planes are circled. a2)-d2) are the Schmid factors of 12 slip systems for the orientation in DBs.

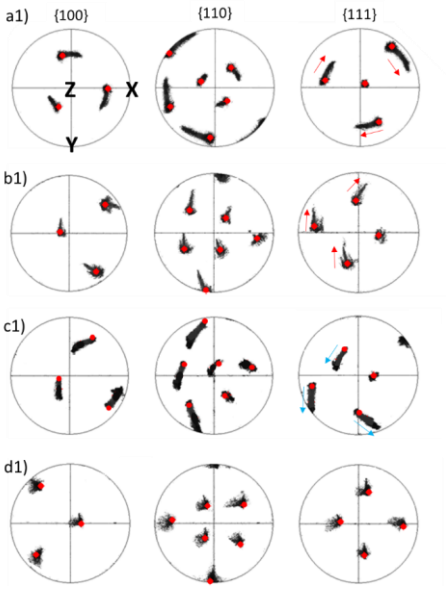

Figure B Pole figures of deformed single crystal a-d. Red dots show the orientation before compression. Red arrows represent the clockwise rotation and blue arrows represent anti-clockwise rotation around Z-axis.

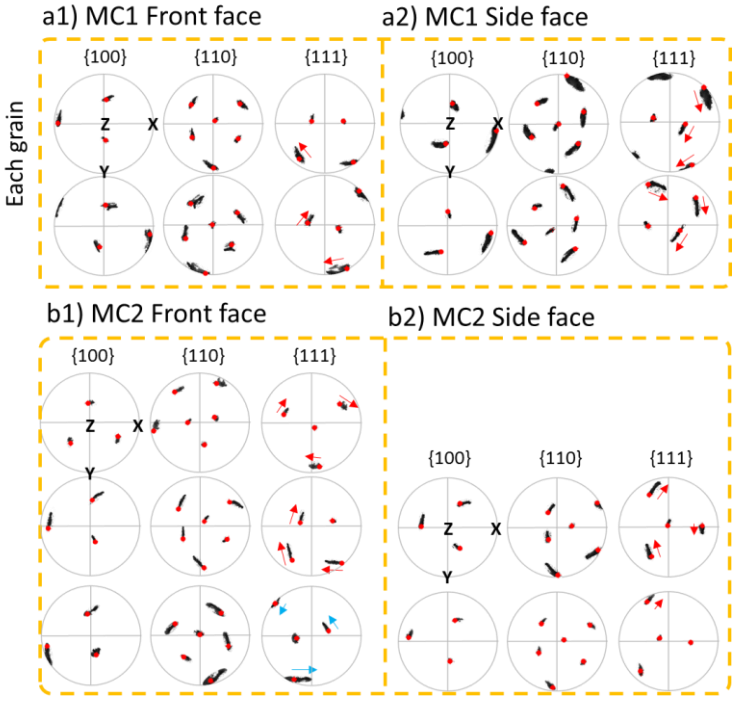

Figure C a1)-a2) and b1)-b2) are PF of each grain in the front and side face of deformed samples. Red dots in PF show the orientation of each grain before compression. Red and blue arrows indicate the clockwise and anti-clockwise rotation of crystal orientation around z-axis during deformation.

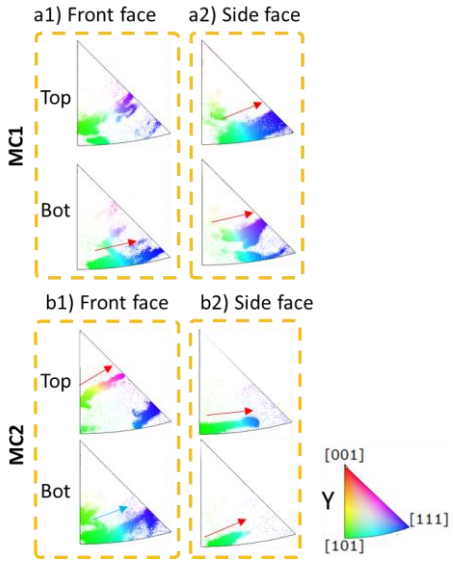

Figure D a1)-a2) and b1)-b2) are the IPF-Y of front and side face on deformed MC 1 and 2. The top and bottom parts are split for the IPF plotting of each face. Colours are consistent with the IPF-Y maps shown in Figure 9.

References

[1] C.S. Barrett, L.H. Levenson, Structure of iron after drawing, swaging and elongation in tension, Trans. Aime. 135 (1939) 327–352.

[2] F. Di Gioacchino, J. Quinta da Fonseca, Plastic Strain Mapping with Sub-micron Resolution Using Digital Image Correlation, Exp. Mech. 53 (2013) 743–754. doi:10.1007/s11340-012-9685-2.

[3] J.B. Hess, C.S. Barrett, Structure and nature of kink bands in zinc, JOM. 1 (1949) 599–606. doi:10.1007/BF03398902.

[4] M.M.M. Miszczyk, H. Paul, J.H.H. Driver, P. Drzyma, P. Drzymała, Recrystallization nucleation in stable aluminium-base single crystals : Crystallography and mechanisms, Acta Mater. 125 (2017) 109–124. doi:10.1016/J.ACTAMAT.2016.11.054.

[5] K. Higashida, J. Takamura, N. Narita, J. Takamurat, N. Narita, The Formation of Deformation Bands in f. c. c. Crystals, Elsevier, 1986. doi:10.1016/0025-5416(86)90266-1.

[6] K. Mecke, C. Blochwitz, Saturation Dislocation Structures in Cyclically Deformed Nickel Single Crystals of Different Orientations, Cryst. Res. Technol. 17 (1982) 743–758. doi:10.1002/crat.2170170610.

[7] K. Hagihara, M. Yamasaki, M. Honnami, H. Izuno, M. Tane, T. Nakano, Y. Kawamura,

Philosophical Magazine Crystallographic nature of deformation bands shown in Zn and Mg-based long-period stacking ordered (LPSO) phase Crystallographic nature of deformation bands shown in Zn and Mg-based long-period stacking ordered (LPSO) phase, (2014). doi:10.1080/14786435.2014.987843.

[8] Y. Yang, L. Wang, T.R. Bieler, P. Eisenlohr, M.A. Crimp, Quantitative Atomic Force Microscopy Characterization and Crystal Plasticity Finite Element Modeling of Heterogeneous Deformation in Commercial Purity Titanium, Metall. Mater. Trans. A. 42 (2011) 636–644. doi:10.1007/s11661-010-0475-0.

[9] F.J. Humphreys, M. Hatherly, Recrystallization and related annealing phenomena, Elsevier, 2004. doi:10.1016/B978-008044164-1/50014-1.

[10] D.M. Moon, W.H. Robinson, DISLOCATION DISTRIBUTION IN DEFORMED SILVER SINGLE CRYSTALS, Can. J. Phys. 45 (1967) 1017–1030. doi:10.1139/p67-074.

[11] J.W. Steeds, Dislocation arrangement in copper single crystals as a function of strain, Proc. R. Soc. London. Ser. A. Math. Phys. Sci. 292 (1966) 343–373. doi:10.1098/RSPA.1966.0139.

[12] F. Basson, J.H. Driver, Deformation banding mechanisms during plane strain compression of cube-oriented f.c.c. crystals, Acta Mater. 48 (2000) 2101–2115. doi:10.1016/S1359-6454(00)00042-2.

[13] R.D. Doherty, D.A. Hughes, F.J. Humphreys, J.J. Jonas, D.J. Jensen, M.E. Kassner, W.E. King, T.R. McNelley, H.J. McQueen, A.D. Rollett, Current issues in recrystallization: a review, Mater. Sci. Eng. A. 238 (1997) 219–274. doi:10.1016/S0921-5093(97)00424-3.

[14] P.A. Beck, P.R. Sperry, C.S. Smith, J.E. Burke, P.R. Sperry, C.S. Smith, J.E. Burke, Strain induced grain boundary migration in high purity aluminum, J. Appl. Phys. 21 (1950) 150–152. doi:10.1063/1.1699614.

[15] K. Huang, R.E. Logé, A review of dynamic recrystallization phenomena in metallic materials, Mater. Des. 111 (2016) 548–574. doi:10.1016/J.MATDES.2016.09.012.

[16] P.R. Rios, F. Siciliano, H. Ricardo, Z. Sandim, R.L. Plaut, A. Fernando Padilha, Nucleation and growth during recrystallization, Mater. Res. 8 (2005) 225–238. doi:10.1590/S1516-14392005000300002.

[17] D. Raabe, Multiscale recrystallization models for the prediction of crystallographic textures with respect to process simulation, J. Strain Anal. Eng. Des. 42 (2007) 253–268. doi:10.1243/03093247JSA219.

[18] A.D.D. Rollett, M.J.J. Luton, D.J.J. Srolovitz, Microstructural simulation of dynamic recrystallization, Acta Metall. Mater. 40 (1992) 43–55. doi:10.1016/0956-7151(92)90198-N.

[19] I.J. Polmear, Light Alloys, Elsevier, 2005. doi:10.1016/B978-075066371-7/50001-3.

[20] R.J. Asaro, Micromechanics of Crystals and Polycrystals, Adv. Appl. Mech. 23 (1983) 1–115. doi:10.1016/S0065-2156(08)70242-4.

[21] Q. Luan, J. Lee, Z. Zheng, J. Lin, J. Jiang, Static recrystallization study on pure

aluminium using crystal plasticity finite element and phase-field modelling, Procedia Manuf. 15 (2018) 1800–1807. doi:10.1016/J.PROMFG.2018.07.211.

[22] M. Miszczyk, H. Paul, J.H. Driver, C. Maurice, New orientation formation and growth during primary recrystallization in stable single crystals of three face-centred cubic metals, Acta Mater. 83 (2015) 120–136. doi:10.1016/j.actamat.2014.09.054.

[23] H. Hallberg, Approaches to modeling of recrystallization, Metals (Basel). 1 (2011) 16–48. doi:10.3390/met1010016.

[24] W.R. Hibbard, W.R. Tully, The effect of orientation on the recrystallization kinetics of cold-rolled single crystals, AIME TRANS. 221 (1961) 336–343.

[25] M.A. Sutton, W.J. Wolters, W.H. Peters, W.F. Ranson, S.R. McNeill, Determination of displacements using an improved digital correlation method, Image Vis. Comput. 1 (1983) 133–139. doi:10.1016/0262-8856(83)90064-1.

[26] F. Hild, S. Roux, Digital Image Correlation: from Displacement Measurement to Identification of Elastic Properties, Strain. 42 (2006) 69–80. doi:10.1111/j.1475-1305.2006.00258.x.

[27] Q. Luan, T.B.B. Britton, T.-S.T.-S. Jun, Strain rate sensitivity in commercial pure titanium: The competition between slip and deformation twinning, Mater. Sci. Eng. A. 734 (2018) 385–397. doi:10.1016/J.MSEA.2018.08.010.

[28] H.J. Scheel, The Development of Crystal Growth Technology, in: Cryst. Growth Technol., John Wiley & Sons, Ltd, Chichester, UK, n.d.: pp. 1–14. doi:10.1002/0470871687.ch1.

[29] GOM Correlate Professional V8 SR1 Manual Basic Inspection-3D Testing, 2015. www.gom.com (accessed July 31, 2019).

[30] Y. Guan, B. Chen, J. Zou, T. Ben Britton, J. Jiang, F.P.E.E. Dunne, Crystal plasticity modelling and HR-DIC measurement of slip activation and strain localization in single and oligo-crystal Ni alloys under fatigue, Int. J. Plast. 88 (2017) 70–88. doi:10.1016/j.ijplas.2016.10.001.

[31] T. Zhang, D.M. Collins, F.P.E.E. Dunne, B.A. Shollock, Crystal plasticity and high-resolution electron backscatter diffraction analysis of full-field polycrystal Ni superalloy strains and rotations under thermal loading, Acta Mater. 80 (2014) 25–38. doi:10.1016/j.actamat.2014.07.036.

[32] F. Di Gioacchino, J. Quinta da Fonseca, Plastic Strain Mapping with Sub-micron Resolution Using Digital Image Correlation, Exp. Mech. 53 (2013) 743–754. doi:10.1007/s11340-012-9685-2.

[33] L.M. Brown, Dislocation pile-ups, slip-bands, ellipsoids, and cracks, Mater. Sci. Eng. A. 400–401 (2005) 2–6. doi:10.1016/J.MSEA.2005.03.043.

[34] K.P. Boyle, Latent Hardening in Copper and Aluminium Single Crystals, Mater. Sci. Forum. 495–497 (2005) 1043–1048. doi:10.4028/www.scientific.net/msf.495-497.1043.

[35] Y. Guo, T.B. Britton, A.J. Wilkinson, Slip band-grain boundary interactions in commercial-purity titanium, Acta Mater. 76 (2014) 1–12.

doi:10.1016/j.actamat.2014.05.015.

[36] S. Birosca, F. Di Gioacchino, S. Stekovic, M. Hardy, A quantitative approach to study the effect of local texture and heterogeneous plastic strain on the deformation micromechanism in RR1000 nickel-based superalloy, Acta Mater. 74 (2014) 110–124. doi:10.1016/J.ACTAMAT.2014.04.039.

[37] J. Jiang, J. Yang, T. Zhang, J. Zou, Y. Wang, F.P.E. Dunne, T.B. Britton, Microstructurally sensitive crack nucleation around inclusions in powder metallurgy nickel-based superalloys, Acta Mater. 117 (2016) 333–344. doi:10.1016/j.actamat.2016.07.023.

[38] J. Jiang, F.P.E.E. Dunne, T. Ben Britton, Toward Predictive Understanding of Fatigue Crack Nucleation in Ni-Based Superalloys, Jom. 69 (2017) 863–871. doi:10.1007/s11837-017-2307-9.